ELSEVIER

Behavior of Cement Based Matrices Reinforced by Randomly Dispersed Microfibers

D.A. Lange,* C. Ouyang,† and S.P. Shah‡
*Department of Civil Engineering, University of Illinois, Urbana, Illinois, †Office of Materials, Iowa Department of Transportation, Ames, Iowa, and ‡Department of Civil Engineering, Northwestern University, Evanston, Illinois

A study on behavior of cement based matrices reinforced by randomly distributed microfibers is summarized. Effects of volume fraction, length and type of fiber, and type of cement based matrix were experimentally examined using uniaxial tensile specimens and three-point bend beams. The matrix fracture properties were measured by a RILEM recommended test procedure. A confocal microscopy technique was used to measure fracture surface roughness, a parameter that was shown to correlate with fracture properties. By incorporating the obtained matrix fracture properties, fiber aspect ratio, and fiber-matrix interface bond into a fracture mechanical R-curve approach, mechanical responses of cement based matrices reinforced by fibers can be predicted. ADVANCED CEMENT BASED MATERIALS 1996, 3, 20–30

KEY WORDS: Cement, Composite materials, Confocal microscopy, Fibers, Fracture, Mortar, Reinforcement, Silica fume

The inherent tensile strength and strain capacity of cement based matrices can be significantly enhanced by using appropriate type and amount of fibers [1]. Very high performance cement based composites were achieved using continuous, long fibers in previous studies [2–5]. Other studies have shown that similar toughening mechanisms also exist when randomly distributed short fibers are used [6–10]. The aim of the current research is to experimentally and theoretically study toughening of cement based matrices reinforced by randomly distributed microfibers that are only 3–6 mm in length.

Experimental Approach

Materials

Two types of cement based matrices were used. The first type of matrix consisted of white portland cement and sand at a ratio of 1:0.5 and is hereafter referred to as the OPC matrix. The second type of matrix was formed by adding 18% silica fume by weight of cement into the OPC matrix and is hereafter referred to as the OPCS matrix. Specific gravities for the white portland cement (Lehigh white cement), the silica fume (Elkem microsilica), and the sand were 3.15, 2.20, and 2.60, respectively. The sand was passed through a no. 30 sieve to remove larger particles. The water:cementitious (cement plus silica fume) ratio was held constant at 0.30 for all mixes. A superplasticizer (W.R. Grace WRDA-19) was added to all mixes in dosages of 100 or 120 cc per batch to improve workability. The mortars were consolidated with the aid of a vibration table. Two types of microfibers made of carbon and steel were used. Microfibers are short fibers with high aspect ratios (e.g. >100) and high specific surface areas (e.g. >200 cm^2/g). Conventional large fibers used in concrete applications are 30–60 mm long with lower specific surface areas. The steel fibers (Novocon International, Inc.) had an average length of 3 mm, a square cross section with an average width of 0.030 mm, a specific surface of 175 cm^2/g, and a specific gravity of 7.6. The carbon fibers (Ashland Petroleum Co.) were pitch-based fibers with an average length of 3 or 6 mm, an average diameter of 0.015 mm, a specific surface of 1650 cm^2/g, and a specific gravity of 1.6.

Mechanical Tests

Two types of specimen geometries, uniaxial tensile dog-bone specimen and three-point bend beam as shown in Figure 1, were used. The tensile specimen had a cross section of 16 × 9 mm and was subjected to a uniaxial tensile load in a universal test machine (MTS). Axial deformation of the specimens was measured using a 12 mm range LVDT, and the gauge length was 76 mm. This deformation was used as a feedback to control loading rate. Both ends of the tensile specimen were reinforced by aluminum plates (0.5-mm thick). The aluminum plate at each end was extended 2 mm into the

Address correspondence to: David A. Lange, Department of Civil Engineering, University of Illinois, 2207 Newmark CE Laboratory, 205 North Mathews, Urbana, Illinois 61801.
Received August 4, 1994; Accepted May 5, 1995

ISSN 1065-7355/96/$15.00
SSDI 1065-7355(95)00032-M

Advn Cem Bas Mat
1996;3:20–30

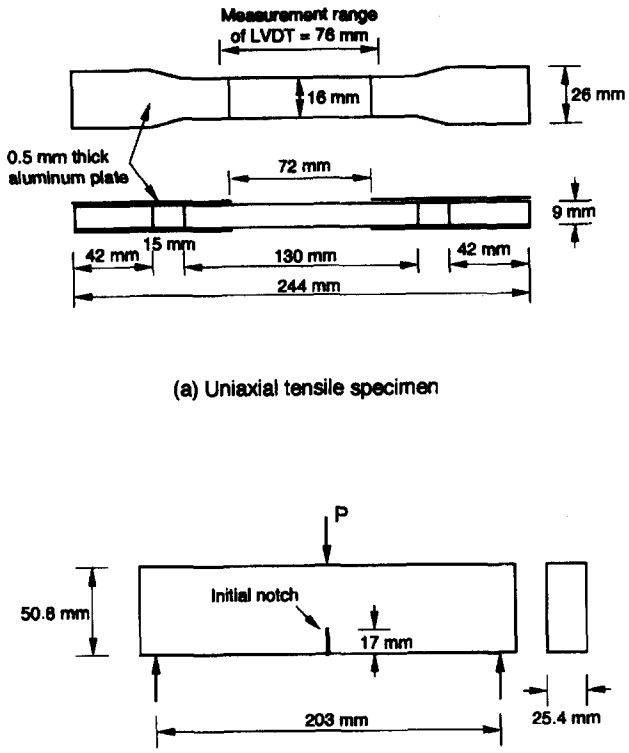

FIGURE 1. Two types of specimen used in the study: (a) uniaxial tensile strength and (b) three-point bend beam.

measurement range of the linear voltage differential transducer (LVDT) to ensure that the specimen would not fail outside the range of the linear voltage differential transducer (LVDT). The three-point bend beam had a dimension of 210 × 50.8 × 25.4 mm. The span of the beam was 203 mm. A notch of 17 mm was cast into the beam. Crack mouth opening displacement (CMOD) was measured using a clip gauge with a gauge length of 5 mm. The signal from the clip gauge was used as a feedback to control loading.

The testing program is summarized in Table 1. Effects of fiber volume fraction, fiber length, fiber type and matrix type on mechanical behavior of the cement based composites were experimentally examined. All tests were conducted on 28-day-old specimens cured in lime water. Results of the tension and bending tests are reported in Tables 2 and 3, respectively.

TABLE 1. Experimental program

Test Series	Matrix Type	Fiber Volume	Fiber Type	Nominal Fiber Length
B	OPCS	0	NA	NA
C	OPCS	2%	Carbon	3 mm
D	OPCS	4%	Carbon	3 mm
E	OPC	4%	Carbon	3 mm
F	OPCS	4%	Carbon	6 mm
G	OPCS	2%	Carbon	6 mm
H	OPCS	4%	Steel	3 mm
I	OPC	0	NA	NA

Microscopy

Scanning electron microscopy and confocal microscopy were used to study the fracture surfaces of the specimens. SEM micrographs provided qualitative information about fiber-matrix bond and fiber pull-out. Confocal microscopy was used to quantify fracture surface roughness by a technique described in detail elsewhere [11]. Roughness of fracture surfaces has been shown to correlate with fracture parameters of plain pastes and mortars [12]. The technique uses the capability of the confocal microscope to optically section the sample and construct a three-dimensional topographic map of the surface. A 256 × 256 digital image is created in which the pixel values represent z-height at the discrete x–y coordinates. Figure 2 shows a typical fracture surface map.

Two sets of confocal images were acquired using a Zeiss laser scanning confocal microscope. First, a relatively low magnification set was acquired from typical samples of all eight mix designs. Nine images were acquired from each of the eight samples. The low magnification set used rectangular pixels to produce a rectangular image measuring 2.1 × 3.2 mm, large enough to encompass the larger features of the fracture surface such as exposed sand grains and protruding fibers. The purpose of this set of images was to determine a roughness number (RN) to represent the tortuosity of the main crack path.

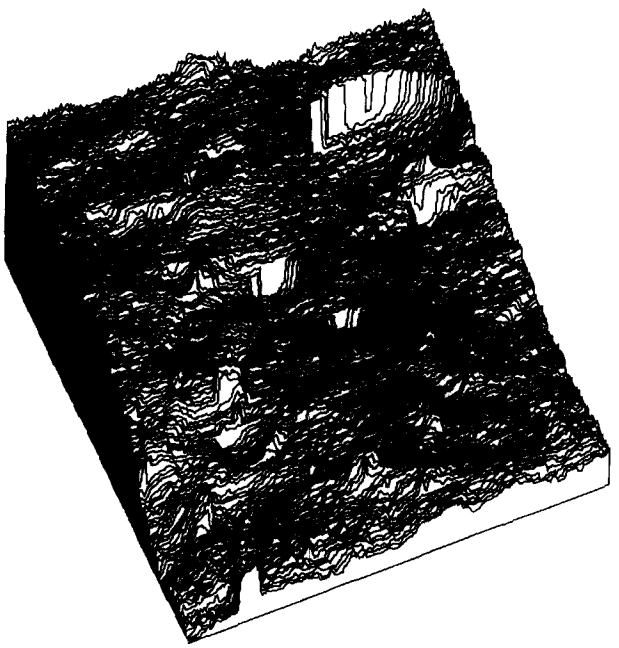

FIGURE 2. Map of fracture surface of mortar with 4% steel microfibers.

TABLE 2. Experimental and analytical results for tension specimens

Mortar Series No.	Specimen No.	Experimental Results: Peak Stress from Test (MPa)	Experimental Results: Strain at Peak Stress	Matrix Peak Stress from Rule of Mixtures (MPa)	Average Matrix Peak Stress from Rule of Mixtures (MPa)	Matrix Peak Stress from R-curve (MPa)
B	B-T1	2.42	0.00021	2.42	2.62	2.96
	B-T2	2.81	0.00022	2.81		
	C-T1	2.97	0.00022	2.99		
C	C-T2	3.13	0.00018	3.16	3.47	3.65
	C-T3	4.22	0.00026	4.25		
	D-T1	3.66	0.00055	3.58		
D	D-T2	3.50	0.00044	3.46	3.87	4.08
	D-T3	4.54	0.00038	4.57		
E	E-T1	2.30	0.00028	2.28	2.83	3.32
	E-T2	3.32	0.00018	3.38		
F	F-T1	6.55	0.00031	6.69	6.23	4.97
	F-T2	5.65	0.00031	5.76		
	G-T1	4.54	0.00033	4.57		
G	G-T2	3.52	0.00026	3.54	3.98	3.81
	G-T3	3.83	0.00031	3.84		
	H-T1	7.33	0.00036	6.89		
H	H-T2	4.26	0.00025	3.92	5.07	4.62
	H-T3	4.86	0.00031	4.42		
	I-T1	2.24	0.00021	2.24		
I	I-T2	2.53	0.00027	2.53	2.46	2.83
	I-T3	2.61	0.00029	2.61		

A second set of confocal images was acquired to investigate the roughness of the matrix in specimens with fiber reinforcement. Thirty images each were acquired from a typical plain OPCS sample (Series B), a sample with 4% carbon fibers (Series D), and a sample with 4% steel fibers (Series H). A relatively high magnification (12.5× higher than the low magnification) was used to capture images of the matrix between the fibers. In this set, square pixels were used to produce a square image measuring 0.2 × 0.2 mm, small enough to view matrix between fibers without including the fibers themselves in the images. The locations of all images were determined in a random manner, but in the case of some high magnification images, the sample may have been selectively moved to remove fibers from the field of view.

A computer program was written to filter and analyze the roughness of the digital image. Both sets of confocal images were smoothed with a 3 × 3 median filter to reduce noise before computation of RN. The pixel values in the image were used to triangulate the surface, and RN computed as follows:

$$\text{Roughness Number (RN)} = \frac{\text{Estimated actual surface area}}{\text{Nominal surface area}} \quad (1)$$

Higher RN values result from the second set of confocal images because the higher resolution is more sensitive to fine features of the fracture surface and texture of calcium silicate hydrate (C-S-H) and other hydration products. For the first set, the resolution in the x-direction (pixel length) was 12.34 μm, the y-resolution was 8.34 μm, and the z-resolution (slice thickness) was 10 μm. The RN values computed for the first, set, reported as an average of nine images, are listed in Table 4. For the second set, the resolution in the x and y directions was 0.72 μm and the resolution in the z-direction was 2.5 μm. The RN values computed for the second set, reported as an average of 30 images, are listed in Table 5.

"Rule of Mixtures" Analysis of Load Resisted by Matrix

Uniaxial Tension

By assuming that measured deformations in fibers and matrix are the same, the stress resisted by a matrix subjected to uniaxial tension can be obtained from the rule of mixtures as:

$$\sigma_m = \frac{\sigma_c - \eta V_f E_f \epsilon}{1 - V_f} \quad (2)$$

where σ_c and σ_m are the stresses resisted by the composite and the matrix respectively, E_f is Young's modulus of the fiber, V_f is the fiber volume fraction, ϵ is the

TABLE 3. Experimental and analytical results for three-point bend specimens

Mortar Series No.	Specimen No.	Experimental Results: Peak Load from Test (N)	Experimental Results: CMOD at Peak Load (mm)	Matrix Peak Load from Rule of Mixtures (N)	Average Matrix Peak Load from Rule of Mixtures (N)	R-curve Prediction for Toughened Matrix: Peak Load (N)	R-curve Prediction for Toughened Matrix: Critical Crack Length (mm)
	B-B1	472	0.013	472			
B	B-B2	522	0.012	522	509	445	18.95
	B-B3	533	0.014	533			
	C-B1	700	0.057	660			
C	C-B2	645	0.058	604	606	520	24.40
	C-B3	600	0.065	554			
	D-B1	620	0.088	495			
D	D-B2	700	0.091	571	564	605	24.55
	D-B3	730	0.073	627			
	E-B1	680	0.042	621			
E	E-B2	590	0.036	539	550	513	24.20
	E-B3	550	0.043	489			
	F-B1	835	0.048	767			
F	F-B2	1080	0.057	999	948	1008	24.75
	F-B3	1150	0.052	1076			
G	G-B1	1020	0.051	984	935	702	24.60
	G-B2	920	0.048	886			
H	H-B1	1400	0.061	968	897	892	24.80
	H-B2	1250	0.060	826			
	I-B1	448	0.014	448			
I	I-B2	430	0.013	430	446	420	19.20
	I-B3	459	0.016	459			

experimentally measured average strain value, and η is the fiber efficiency factor depending on many factors including orientation, dimension, and stiffness of fiber as well as fiber-matrix interface bond. A value of η = 0.25 was used. The Young's modulus for the steel fiber was 200 GPa and for the pitched-based carbon fiber was 40 GPa. Matrix peak loads computed for the uniaxial tension specimens are reported in Table 2.

Bending

The cross section of a composite beam can be separated into a fiber portion and a matrix portion. For given values of composite load, P, and CMOD, the corresponding crack length can be calculated from linear elastic fracture mechanics (LEFM) formulation,

$$\text{CMOD} = \frac{6Psa}{E_c b^2 t_c} V_1\left(\frac{a}{b}\right) \tag{3}$$

$$V_1\left(\frac{a}{b}\right) = [0.76 - 2.28\left(\frac{a}{b}\right) + 3.38\left(\frac{a}{b}\right)^2 - 2.04\left(\frac{a}{b}\right)^3 + \frac{0.66}{(1 - a/b)^2}] \tag{4}$$

where t_c and E_c are thickness and Young's modulus of the composite beam section, s and b are span and depth of the beam, and a is the crack length (see Figure 1b).

Because the fiber portion and the matrix portion of

TABLE 4. Roughness of specimens

Series No.	Average Roughness Number	Standard Deviation of Roughness Number
B	1.618	0.075
C	1.844	0.061
D	2.419	0.288
E	1.983	0.124
F	2.137	0.399
G	1.778	0.067
H	2.151	0.619
I	1.641	0.050

TABLE 5. Roughness of matrix adjacent to fibers

Series No.	Fiber Type and Content	Average Roughness Number	Standard Deviation of Roughness Number
B	plain OPCS matrix	3.317	0.311
D	4% carbon (3 mm)	5.466	0.570
H	4% steel (3 mm)	4.239	0.624

the beam have the same deformation and crack extension under the assumption of equal strains, the load resisted by the fiber portion, P_f, can be estimated after knowing the values of CMOD and the corresponding crack length at different load levels,

$$P_f = \frac{E_f b^2 t_f \text{CMOD}}{6saV_1\left(\frac{a}{b}\right)} \tag{5}$$

where E_f is the Young's modulus of the fiber, $t_f = \eta b V_f$ is the effective thickness of the fiber portion of the beam, and η is the fiber efficiency factor.

Load resisted by the matrix portion can be obtained by subtracting the load resisted by the fiber portion from the measured composite load.

Since the value of E_f (=40 GPa) for carbon fibers is close to the value of E_m (=27 GPa for the OPCS matrix), the obtained stress or load resisted by the matrix is almost equal to that resisted by the composite for carbon fiber reinforced composites. However, for steel fiber composites, the obtained matrix stress or load is smaller than that by the composite because E_f = 200 GPa.

Matrix peak loads computed for the bending specimens are reported in Table 3.

Experimental Results

Effect of Fiber Volume Fraction

The effect of fiber volume fraction can be seen in comparisons of Series C (V_f = 2%, 3-mm carbon fibers) with Series D (V_f = 4%, 3-mm carbon fibers) and Series G (V_f = 2%, 6-mm carbon fibers) with Series F (V_f = 4%, 6-mm carbon fibers). Figure 3 shows typical mechanical response from the bend tests for specimens with different fiber volume fraction. Calculated values of matrix contribution is plotted in Figure 3. Higher fiber volume fraction had the effect of increasing matrix peak stress and increasing strain to peak in the tensile tests and flexure tests.

The fracture surface roughness number was significantly higher for specimens with higher volume fraction of fibers. This increase in roughness was very evident by visual observation. It should be noted that, in general, the standard deviation of the roughness data was much higher for high roughness series than for low roughness series.

Effect of Fiber Length

The effect of fiber length can be seen in comparisons of Series C (3 mm) with Series G (6 mm) and Series D (3 mm) with Series F (6 mm). Figure 4 from uniaxial tension tests shows measurable differences in the mechanical response of matrix contribution with different fiber lengths. In both the C/G and D/F comparisons, greater energy absorption (area under the stress-strain curve) was evident in specimens with longer fiber length. The D/F comparison indicated that greater peak load resulted from longer fiber length.

Fracture surface roughness did not increase as fiber length was increased. Series C and G were similar in roughness, whereas Series D was actually somewhat rougher than Series F.

Effects of Matrix Type

The effect of matrix type can be seen in comparisons of Series B and I (both with no fibers) and Series D and E (both with 4% of 3-mm carbon fibers). There was small improvement in peak load by the use of silica fume in the Series B mortar when compared to the plain Series I mortar, but no significant difference in strain to peak was observed. The OPCS matrix in Series D led to im-

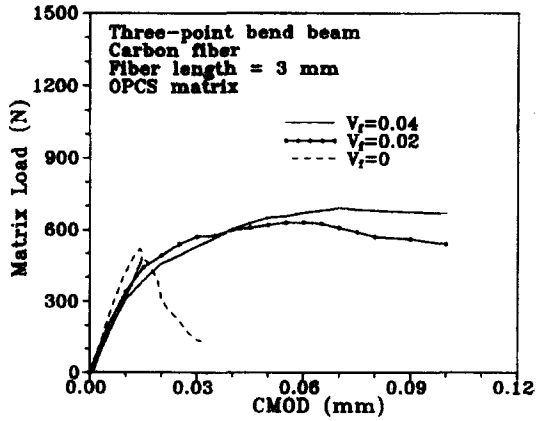

FIGURE 3. Effect of fiber volume fraction: matrix load versus CMOD from bending tests (Series B, C, and D).

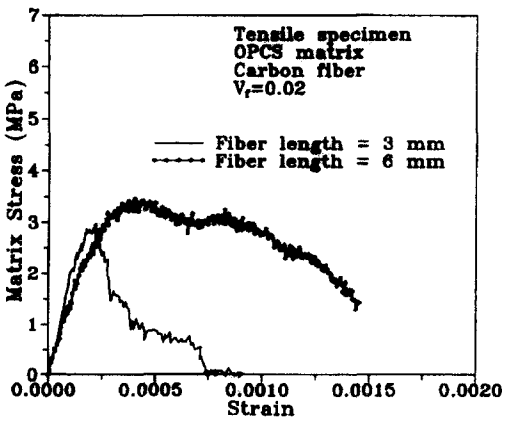

FIGURE 4. Effect of fiber length: matrix stress versus strain from uniaxial tension tests (Series C and G).

provements in carbon fiber reinforced matrices. Figure 5 from bend tests illustrates the Series D/E comparison. Series D achieved higher peak load and strain to peak than Series E.

The surface roughness measurements reflected the differences in behavior in the B/I and D/E comparisons. There was little difference in mechanical response in the B/I comparison, and the roughness measurements were similar for Series B and I specimens. Series D had greater roughness than Series E, reflecting the improvements in mechanical properties due to incorporation of silica fume in the matrix. Silica fume is known to densify the matrix and improve matrix-fiber interfacial bond resulting in improved properties.

Effect of Fiber Type

The effect of fiber type can be seen in comparisons of Series D (carbon) and H (steel). Figure 6 shows that the steel fibers were much more effective in strengthening the mortar specimens in bend tests. The peak load of Series H was almost twice that of Series D. However, the strain to peak load was higher for Series D than for Series H.

Analysis of surface roughness showed that the fracture of Series D (carbon) involved a much more tortuous crack path. Although Series H was clearly stronger and tougher, its fracture surface had much lower roughness. Results of both the low magnification confocal images (Table 4) and high magnification confocal images (Table 5) showed greater roughness for Series D.

Discussion of Experimental Results

It has been recognized that fibers can enhance toughness of fiber reinforced concrete. The presence of fibers will constrain opening of matrix macrocracks thereby enhancing the postpeak response of the composite.

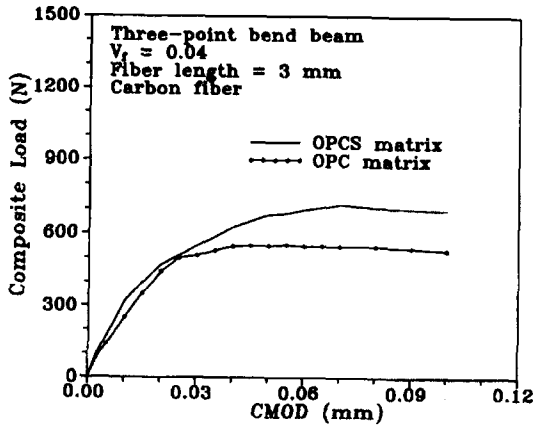

FIGURE 5. Effect of matrix type: composite load versus CMOD from bending tests (Series D and E).

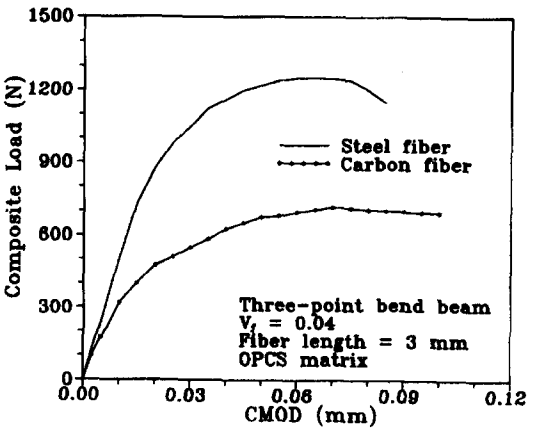

FIGURE 6. Effect of fiber type: composite load versus CMOD from bending tests (Series D and H).

In this case, additional toughening is attributed to debonding and pulling out of fibers.

Fibers can also improve the prepeak response and enhance the matrix tensile strength, if they can effectively bridge matrix microcracks. The effectiveness of the fiber-bridging action will depend on the length, diameter, and distribution of fibers as well as on fiber-matrix properties. With the relatively small volume of fibers used in fiber reinforced concrete, the commonly used fibers are too widely spaced to influence the prepeak response of the matrix. However, if microfibers (fiber diameter in micron range) are used, then it is possible even with the relatively smaller volume of fibers to enhance the tensile strength of the matrix. This is demonstrated by the results of the research reported here. As shown in Tables 2 and 3, the matrix tensile strength (calculated using the rule of mixtures) is substantially enhanced when microfibers are used.

The increase in matrix tensile strength can be explained by fracture mechanics as considered later in this paper. It is assumed that the presence of microfibers alters microstress distribution (such as stress intensity factor) and as a result, higher stresses are required to propagate a crack in the matrix. The matrix fracture toughness is assumed to be unchanged by the presence of fibers. However, the roughness measurements of the study seem to indicate that the presence of fiber can enhance the toughness of the matrix itself.

Results of this study indicated that the roughness of the matrix increases with increasing fiber volume fraction. Increased roughness was observed even when the roughness measurement was made on a micron scale indicating that the matrix roughness itself is altered in the presence of fibers (Table 5). The work by Lange et al. [12] has shown that the roughness number correlated well with the fracture toughness of the matrix. Zampini et al. [13] has recently shown that incorporation of sand particles increases the roughness of cement matrix. The

increased roughness was also related to the increased toughness. Furthermore, the increased roughness of the fracture surfaces was concentrated primarily in the interfacial zone between the bulk matrix and the sand particle. It is postulated that the increased roughness of the matrix observed in the current study is associated with the fiber-matrix interface. When a higher fiber volume fraction is used, a larger area of interface is involved. As a result, it was observed that increasing the volume of fibers increased the roughness of the matrix.

The fact that the improved toughness of the matrix is associated with the increased roughness of the interfacial zone can also be deduced from the results of specimens that incorporated silica fume as well as when the effect of fiber type is analyzed. Incorporation of silica fume did not alter the roughness of unreinforced matrix. However, when fibers were used, the incorporation of silica fume substantially increased the roughness of the matrix. It is known that silica fume densifies the fiber-matrix interface. Thus, the increased roughness of the matrix when both fibers and silica fume are present is due to the increased toughness of the interfacial zone.

One important difference between the two fiber types is that carbon fibers had smaller diameters and were more numerous than the steel fibers for a given mortar volume. The carbon fibers had a specific surface about 10 times greater than the steel fibers. Therefore, specimens reinforced with carbon fibers had a relatively higher proportion of interfacial zone. This is reflected in the roughness of the matrix in specimens reinforced with carbon fibers as compared with those with steel fibers.

Although the matrix toughness as indicated by the roughness measurement was higher for carbon fiber specimens, the maximum tensile strength capacity of the matrix reinforced with carbon fibers was lower than

FIGURE 7. Carbon fiber has relatively smooth surface texture (Series C).

FIGURE 8. Steel fiber has relatively coarse surface texture (Series H).

that with steel fibers (as calculated by the rule of mixtures). This is perhaps the result of more efficient bridging of microcracks provided by steel fibers. The relative efficiency of the two types of fiber is related to their surface textures. Carbon fiber had a relatively smooth surface texture (Figure 7), whereas the steel fiber surface had greater roughness (Figure 8).

The efficiency of fibers during bridging depends both upon bond characteristics and the embedment length of fibers. Calculated matrix tensile strength increased with increasing length of fibers. However, as expected, the length of fibers have no influence on the measured roughness of the matrix. An analysis of the relationship between composite strength and roughness number is presented next.

In summary, the benefits of fibers in cement based composites may be attributed to three mechanisms. First, fibers that bridge microcracks create closing pressures that suppress crack growth. Second, the presence of small, closely spaced microfibers induces improved matrix behavior through crack deflection. Third, fibers that span opening macrocracks will debond and pullout (or break) thereby enhancing postpeak load behavior. The first two of these three mechanisms are particularly relevant to prepeak load behavior. A theoretical model for prediction of the bridging effect of microfibers is described later in this paper.

Analysis of Relationship Between Composite Strength and Roughness Number

Figure 9 shows peak bending load plotted against RN for the control and carbon fiber reinforced specimens.

Figure 9 illustrates that fiber length is a significant factor affecting composite strength. A simple analysis approach has recently been proposed by Betterman et al. [14] to account for the effect of fiber length. This approach is briefly presented and used here.

In fiber-reinforced matrices, the fibers usually provide bridging across the cracked surfaces of the matrix. The bridging force can be evaluated by pulling a fiber out of the matrix. Therefore, it is reasonable to assume that the peak load is proportional to the fiber pull-out force. Ouyang et al. [15] have found that since the value of slip corresponding to the peak pull-out load is small, the effect of frictional stress before the peak pull-out load may be neglected. As a result, the peak pull-out force is the force necessary to debond the fiber and may be expressed as

$$P_c^2 = \frac{8\Gamma E_f \pi^2 r^2}{\coth^2[\omega(L - a_c)]} \tag{6}$$

where P_c is the peak pull-out force, Γ is the surface energy for debonding, r is the radius of the fiber, ω is the interfacial material parameters, L is the embedment length of the fiber, and a_c is the debonded length corresponding to the peak pull-out force. Therefore, the ratio of pull-out forces for two different fibers is

$$k_{12} = \frac{P_{c1}}{P_{c2}} = \left(\frac{r_1}{r_2}\right)^{3/2} \frac{\coth[\omega(L_2 - a_{c2})]}{\coth[\omega(L_1 - a_{c1})]} \tag{7}$$

where k_{12} is the length and diameter factor of the fibers, and subscripts 1 and 2 represent two fibers of the same type that may have different geometry and embedment lengths. It is assumed that the value of ω is equivalent for the same type of fiber and matrix. In this investigation, a value of ω = 133 m^{-1} previously measured [14] was used. Analysis detailed in Ouyang et al. [15] indicates that the peak load usually occurs when the debonded length of the fiber is 0.75 L to 0.85 L. Therefore, the value of the critical debonded length a_c was assumed to be 0.8 L for simplicity.

To compute the pull-out force ratios for the fibers used in this investigation, the 3- and 6-mm long fibers were designated as fibers 1 and 2, respectively. The 3-mm long fiber was used as a reference fiber for comparison purposes. Hence, k_{11} = 1. By substituting values of L and ω for the three different fibers into eq 7, the value of k_{12} = 0.503 was obtained. The values of the peak bending load for the specimens reinforced with 6-mm long fiber were then multiplied by the factor k_{12} = 0.503. The resulting values of the normalized peak load were then plotted against maximum fiber distance

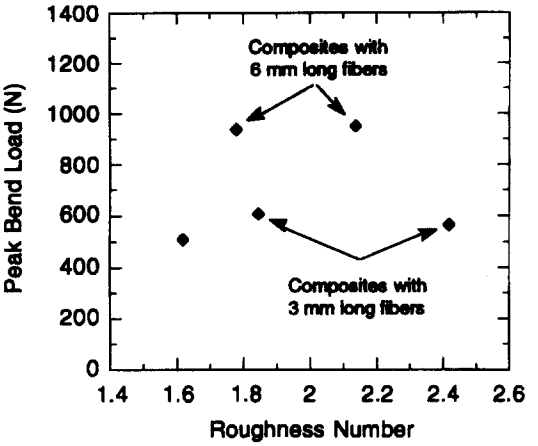

FIGURE 10. Normalized peak bending load versus roughness number for specimens with different fiber length (Series B, C, D, F, and G).

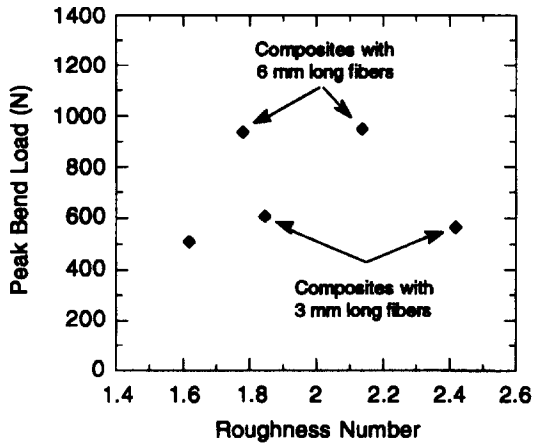

FIGURE 9. Peak bending load versus roughness number for specimens with different fiber length (Series B, C, D, F, and G).

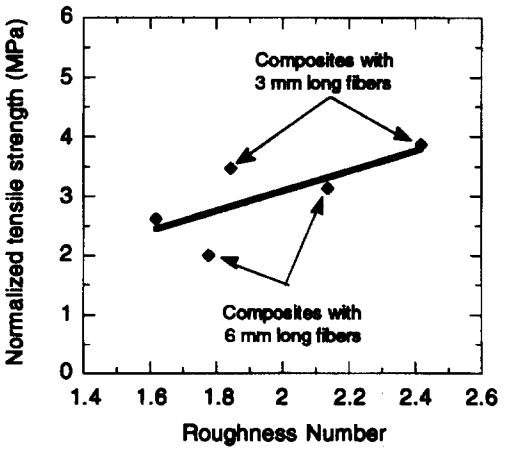

FIGURE 11. Normalized strength versus roughness number for specimens with different fiber length (Series B, C, D, F, and G).

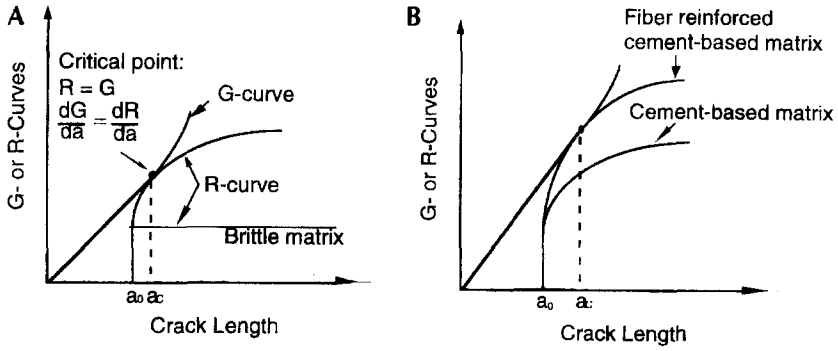

FIGURE 12. R-curves for plain and reinforced cement based materials. (A) Plain matrix, (B) fiber-reinforced matrix.

as shown in Figure 10. Figure 10 shows that normalized peak loads are basically a unique function for composites reinforced by fibers with different lengths. A similar procedure was applied to the peak tensile strength, and the obtained results are shown in Figure 11.

This analysis demonstrates that the superior properties of specimens with longer fibers is due primarily to the greater load required for fiber debonding. The confocal technique observes the fracture surface but cannot "see" the debonded zones (i.e., the sockets left from fiber pull-out) that extend away from the fracture surface into the matrix. Consequently, RN did not increase with increasing fiber length.

Predictions of Bridging Effect of Microfibers

An R-curve type model has been proposed to predict toughening of cement based matrices due to fiber reinforcement [16]. This R-curve approach is briefly reviewed here.

When load is applied to a specimen with an initial flaw of size a_o, it produces strain energy (U). The rate of strain energy release with respect to crack length (a) is denoted by G and is referred to as strain energy release rate. Crack propagation at the crack tip consumes some energy (W). Rate of change of this energy with respect to crack length (a) is denoted by R and is referred to as the fracture resistance. The crack propagates when the following condition is satisfied:

$$G = R \tag{8}$$

For an ideally brittle material, R is a material constant, and propagation of the initial flaw may mean catastrophic failure of the specimen. However, in cementitious materials, due to the existence of crack arrest mechanisms such as aggregate bridging, the crack steadily propagates until a second condition is also satisfied (see Figure 12a):

$$\frac{\partial G}{\partial a} = \frac{\partial R}{\partial a} \tag{9}$$

To use eqs 8 and 9 to describe critical crack propagation, an R-curve formulation should be known. An approximate R-curve previously proposed is expressed as [17]

$$R = \beta(a - a_o)^d \tag{10}$$

$$d = \frac{1}{2} + \frac{\alpha - 1}{\alpha} - \left[\frac{1}{4} + \frac{\alpha - 1}{\alpha} - \left(\frac{\alpha - 1}{\alpha}\right)^2\right]^{1/2} \tag{11}$$

where $\alpha = a_c/a_o$, and β is a constant to be determined. The values of α and β can be obtained from the matrix fracture properties: K_{IC} and $CTOD_C$, where K_{IC} is the critical stress intensity factor and $CTOD_C$ is the critical crack tip opening displacement. The values can be determined from a single notch beam test [18].

Figure 12 illustrates that the fibers provide additional toughening to cement based materials. This fiber toughening can be taken into account by a closing pressure. For randomly distributed short fibers, the following relationship between the closing pressure and the slip displacement is assumed [9]:

$$p = \frac{p_o u}{u_o} \tag{12}$$

where u is the fiber slip that is equal to half the crack opening displacement, p_o is the maximum pull-out load, and u_o is the fiber slip at the maximum pull-out load. The value of p_o is given by

$$p_o = \frac{\eta \tau V_f L}{d_f} \tag{13}$$

where L is the fiber length, d_f is the fiber diameter, and τ is the average bond strength of fibers.

As a result, the conditions for the critical crack propa-

gation, which corresponds to the peak matrix load for matrices with fiber reinforcement, are

$$K_{IC} = K_I^m(\sigma_{mf}, a_c) - \int_0^{a_c} p(x,a_c)K_I^F(x,a_c)dx \quad (14)$$

$$\text{CTOD}_c = \text{CTOD}_m(\sigma_{mf}, a_c, a_o) - \int_{a_o}^{a_c} p(x,a_c)Q(\sigma_{mf}, a_c, a_o)dx \quad (15)$$

where σ_{mf} is the peak stress resisted by the toughened matrix, Q is the Green's function for the crack closure at point a_o due to a unit force applied at point x along the crack length, p is the closure pressure at a point s along the crack face, and K_I^F is the stress intensity due to a unit load applied at the point x along the crack surface. K_I^m, CTOD_m, K_I^F, and Q can be obtained by LEFM [19]. Two unknowns, σ_{mf} and a_c, can be obtained from eqs 14 and 16. Parameters α and β can then be determined, and the mechanical response of matrices reinforced by fibers can be predicted.

To predict the peak load of cement based matrices due to fiber reinforcement, the material properties E_m, K_{IC}, and CTOD_C were first measured using the same dimension beams made of plain unreinforced matrices. The values of E_m = 24 GPa, K_{IC} = 18 N/mm$^{-3/2}$, and CTOD_C = 0.003 mm were obtained for the OPC matrix. The values of E_m = 27 GPa, K_{IC} = 23 N/mm$^{-3/2}$, and CTOD_C = 0.006 mm were obtained for the OPCS matrix. The values of η = 0.25, τ = 1.5 MPa, and u_o = 0.006 mm were used for the OPCS matrix reinforced by the carbon fiber.

Theoretical and experimental comparisons for the OPCS matrix reinforced by the carbon fiber are shown in Figure 13 for tensile specimens and in Figure 14 for the three-point bend beam specimens. Values of matrix peak load and critical crack length computed by the R-curve approach are shown in Tables 2 and 3. The proposed R-curve approach provides results that match quite well with the experimental results. One of the strengths of the proposed R-curve approach is that it permits prediction of the fracture response of different geometries from a given set of material properties.

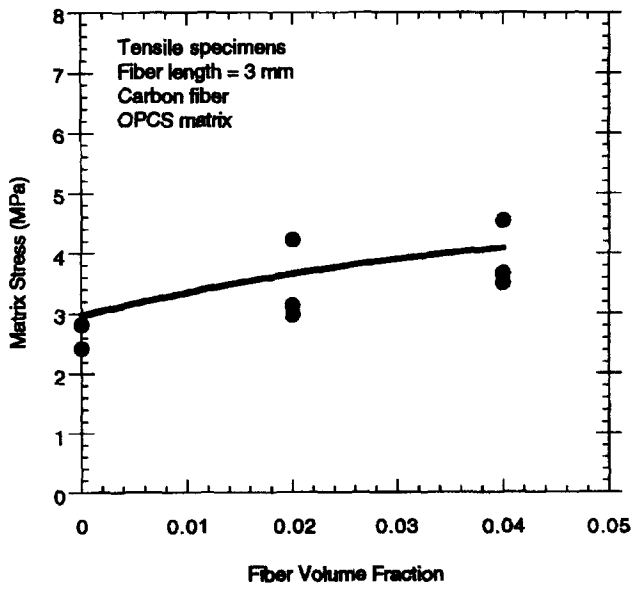

FIGURE 13. Theoretical versus actual matrix stress of specimens in uniaxial tension (Series B, C, and D).

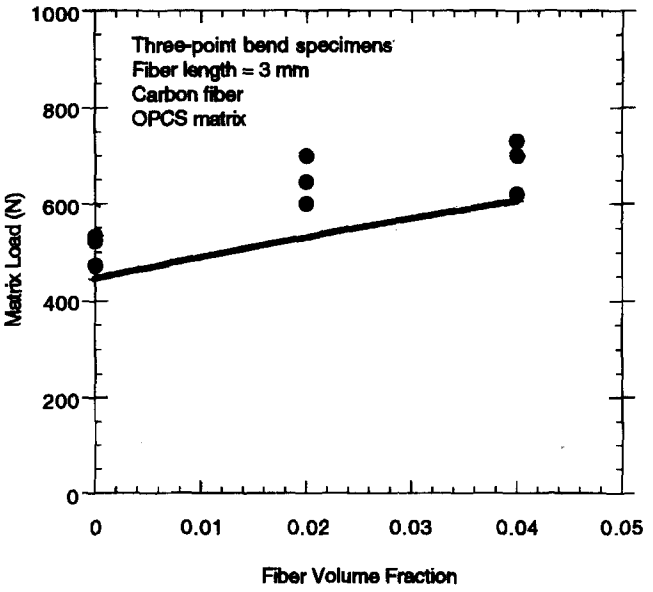

FIGURE 14. Theoretical versus actual matrix load of specimens in bending (Series B, C, and D).

Summary

This study has investigated carbon and steel microfiber mortars. The experimental results illuminated effects of fiber volume fraction, fiber length, matrix type, and fiber type. Increases in fiber volume fraction and longer fiber length resulted in enhanced properties. The matrix with silica fume generally outperformed the plain matrix in fiber reinforced specimens. The steel fibers contributed more to properties than did carbon fibers due to ductility of and surface texture of the steel fibers.

The confocal technique produced digital maps of fracture surfaces that quantify greater crack path tortuousity present in microfiber reinforced specimens than in the unreinforced control specimens. The analysis of fracture surface roughness demonstrated that roughness number generally correlated with fracture properties of fiber reinforced systems. However, the relationship between fiber length and roughness was an exceptional case in which roughness did not correlate with changes in material properties. An analysis of the rela-

tionship between composite strength and roughness demonstrated that enhanced properties of specimens with longer fibers were due primarily to greater debonded fiber-matrix interface not seen by the confocal technique.

The rule of mixtures analysis differentiated the matrix contribution from the fiber contribution, and it was demonstrated that the presence of fibers enhances the contribution of the matrix. In fiber reinforced mortars, there is a synergistic effect whereby the composite performance is greater than the sum of the expected fiber contribution and the performance of plain matrices. Indeed, the matrix contribution computed from the rule of mixtures analysis was always substantially higher than properties measured using plain matrix specimens. This finding is supported by physical evidence from the high magnification confocal images. The high magnification set showed much higher roughness in matrix adjacent to fibers than in matrix of unreinforced specimens. The higher roughness adjacent to fibers indicates that the fibers deflect cracks and stimulate toughening mechanisms in the nearby matrix.

The R-curve approach to analysis of fracture properties was successfully applied and can be used for prediction of composite behavior given fiber and plain matrix properties. The distinguishing feature of the R-curve approach is that it uses matrix properties K_{IC} and $CTOD_C$ that characterize nonlinear fracture behavior of quasibrittle materials.

Acknowledgment

The authors gratefully acknowledge support from the National Science Foundation Center for Advanced Cement-Based Materials (ACBM), Evanson, Illinois (NSF grant No. DMR 8808432-01).

References

1. Balaguru, P.; Shah, S.P. *Fiber Reinforced Cement Composites;* McGraw-Hill: New York, 1992; pp 530.
2. Shah, S.P. *ACI Mater. J.* **1991,** *88,* 595–602.
3. Mobasher, B.; Shah, S.P. In *Thin-Section Fiber Reinforced Concrete and Ferrocement,* ACI SP-124; American Concrete Institute: Detroit, MI, 1990; pp 136–150.
4. Mobasher, B.; Stang, H.; Shah, S.P. *Cem. Concr. Res.* **1990,** *20,* 665–676.
5. Somayaji, S.; Shah, S.P. *ACI Mater. J.* **1981,** *78,* 217–225.
6. Ohama, Y.; Amano, M.; Endo, M. *Concr. Interntl.* **1985,** Mar. 58–62.
7. Banthia, N.; Sheng, J. In *Proceedings of 2nd Canadian Symposium on Cement and Concrete,* 1991.
8. Park, S.B.; Lee, B.I.; Lim, Y.S. *Cem. Concr. Res.* **1991,** *21,* 589–600.
9. Ouyang, C.; Shah, S.P. *Cem. Concr. Res.* **1992,** *22,* 1201–1215.
10. Banthia, N.; Moncef, A.; Sheng, J. In *Thin Reinforced Concrete Products and Systems,* ACI SP-146; Balaguru, P.N., ed.; American Concrete Institute: Detroit, MI, 1994; pp 43–68.
11. Lange, D.A.; Jennings, H.M.; Shah, S.P. *J. Mater. Sci.* **1993,** *28,* 3879–3884.
12. Lange, D.A.; Jennings, H.M.; Shah, S.P. *J. Am. Ceram. Soc.* **1993,** *76,* 589–597.
13. Zampini, D.; Jennings, H.M.; Shah, S.P. *J. Mater. Sci.* **1994,** in press.
14. Betterman, L.R.; Ouyang, C.; Shah, S.P. *J. Adv. Cem. Based Mater.* **1995,** in press.
15. Ouyang, C.; Pacios, A.; Shah, S.P. *J. Eng. Mech.* **1994,** *120,* 2641–2659.
16. Mobasher, B.; Ouyang, C.; Shah, S.P. *Int. J. Fracture* **1991,** *57,* 199–219.
17. Ouyang, C.; Shah, S.P. *J. Am. Ceram. Soc.* **1991,** *74,* 2831–2836.
18. RILEM Committee on Fracture Mechanics of Concrete. *Mater. Struct.* **1990,** *23,* 457–460.
19. Tada, H.; Paris, P.C.; Irwin, G.R. *The Stress Analysis of Cracks Handbook,* 2nd ed.; Paris Productions: St. Louis, 1985.